Mathematical Medicine and Biology (2017) **00**, 1–23
doi: 10.1093/imammb/dqx007

Flow in the anterior chamber of the eye with an implanted iris-fixated artificial lens

JENNIFER H. TWEEDY[†,‡]
Department of Bioengineering, Imperial College London, London SW7 2AZ, UK
[†]Corresponding author. Email: j.siggers@imperial.ac.uk
[‡]*Note that this author formerly published under the name J. H. Siggers.*

JAN O. PRALITS AND RODOLFO REPETTO
D.I.C.C.A. Department of Civil, Chemical and Environmental Engineering, University of Genoa, Genoa, Italy

AND

PAOLO SOLERI
Ophtec, Groningen, the Netherlands

[Received on 7 March 2016; revised on 21 June 2017; accepted on 21 June 2017]

Flow in the aqueous humour that fills the anterior chamber of the eye occurs in response to the production and drainage of the aqueous humour, and also due to buoyancy effects produced by thermal gradients. Phakic intraocular lenses are manufactured lenses that are surgically inserted in the eyes of patients to correct refractive errors. Their presence has a dramatic effect on the circulation of the aqueous humour, resulting a very different flow in the anterior chamber, the effects of which have not been extensively investigated. In this article we use a simplified mathematical model to analyse the flow, in order to assess the effect of the implanted lens on the pressure drop required to drive the flow and also on the wall shear stress experienced by the corneal endothelial cells and the cells of the iris. A high pressure drop could result in an increased risk of glaucoma, whilst raised shear stress on the cornea could result in a reduction in the density of endothelial cells there, and on the iris it could result in the detachment of pigment cells, which block the outflow of the eye, also leading to glaucoma. Our results confirm those of previous fully numerical studies, and show that, although the presence of the lens causes significant differences in the flow topology and direction, the typical magnitudes of the shear stress are not significantly changed from the natural case. Our semi-analytical solution allows us to perform a thorough study of the dependence of the results on the controlling parameters and also to understand the basic physical mechanisms underlying flow characteristics.

Keywords: eye; fluid mechanics; anterior chamber.

1. Introduction

Aqueous humour in the eye is produced by the ciliary processes, flows radially inward through the posterior chamber, anteriorly through the pupil and then radially outward through the anterior chamber into the angle of the eye, where it flows through the trabecular meshwork, Schlemm's canal and into the collector channels and out of the eye. This flow is considerably disrupted by the placement of a phakic intraocular lens (pIOL), which is an artificial lens used to correct refractive errors such as myopia, astigmatism, hyperopia and presbyopia in patients who are unsuitable for LASIK (laser) surgery and

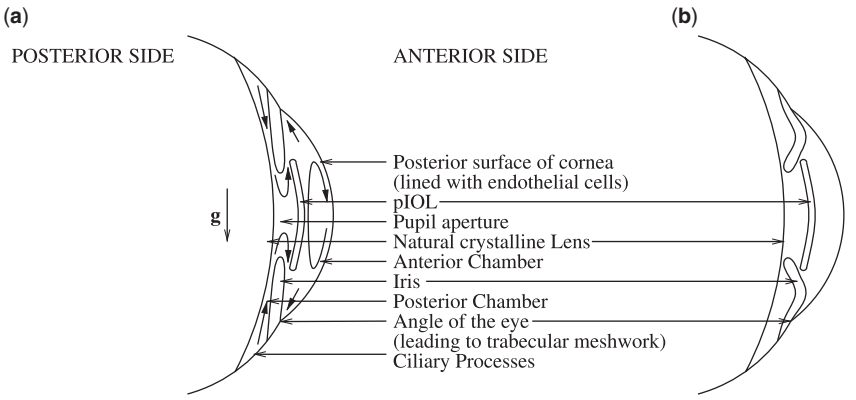

FIG. 1. (a) Schematic diagram of anterior of the eye showing the flow of aqueous humour in the presence of the implanted lens. The anterior and posterior chambers and the pupil aperture are filled with aqueous humour, and the solid-headed arrows indicate the direction of its flow due to the production and drainage of aqueous humour, with the exception of the curved arrow in the region anterior to the pIOL, which indicates the expected flow due to the convection current set up when the subject is upright with eyelids open in a 20°C environment. (b) Schematic diagram indicating the bowed configuration of the iris during angle closure glaucoma.

unwilling to wear glasses or contact lenses. In contrast to aphakic lenses, which are lenses implanted after all or part of the natural crystalline lens has been removed, these lenses do not interfere with the normal working of the natural lens, but rather, as with glasses or contact lenses, they correct the vision, allowing myopics to focus on distant objects. There are three main designs of pIOLs: sulcus-supported lenses, which sit in the posterior chamber between the natural lens and the iris; and angle-supported lenses and iris-fixated lenses, which both sit in the anterior chamber and, as their names suggest, are held in place by haptics that extend into the angle and by haptics with claws that attach to the anterior iris tissue, respectively (Raciti & Majmudar, 2013). In this article we consider an iris-fixated lens, which is an approximately circular, domed disc placed in the anterior chamber and positioned axisymmetrically between the anterior iris and the posterior cornea, see Fig. 1(a), which also indicates the main anatomical features and the pathway of the aqueous humour.

Several studies have been performed to measure ocular surface temperature, with values indicating a normal range of 32.9–36°C (Purslow & Wolffsohn, 2005). The iris contains blood vessels and thus is close to body temperature, meaning that there is a temperature gradient across the anterior chamber, and the buoyancy effects drive a significant flow (shown in Fig. 1(a)). The aqueous humour near the cornea is cooler than that near the iris/natural lens, and so when the subject is upright, the fluid at the posterior surface of the anterior chamber tends to rise, whilst that at the anterior tends to sink, leading to the formation of a buoyancy-driven circulation current in the anterior chamber. This convection current coexists with the flow due to the production and drainage of aqueous humour, which, in the anterior chamber, is predominantly radially outward. In fact, however, in an upright and awake patient the buoyancy-driven flow is typically much stronger than the flow due to the production and drainage (the results in this article will suggest it is stronger by a factor of order 10^2).

As can be seen in Fig. 1(a), the presence of the lens over the pupil significantly disrupts the normal flow pattern, and this has led to concerns over the safety of such devices; in this article we address two of the concerns. Firstly, the shear stress on the iris and cornea could be greater with the lens in place than in the natural situation, which in turn could cause endothelial cells to be pulled away from the cornea (Doors *et al.*, 2010) and pigment cells from the iris. Secondly, the pressure drop between the posterior

chamber and the anterior chamber could increase compared to the natural situation, because of the greater resistance between the ciliary body and the angle of the eye. In turn this could increase the risk of angle closure glaucoma in which this pressure drop is so great that the iris bows forwards, squeezing together the tissues at the angle of the eye and blocking the outflow of aqueous humour, see Fig. 1(b). In this article we develop a mathematical model to predict the likelihood of the occurrence of these phenomena.

There is some previous work on aqueous humour flow from which we shall draw for the present model. Canning *et al.* (2002) developed a theoretical model to calculate the fluid flow in the anterior chamber, which they showed can approximately be written as the sum of two contributions: the flow due to the production of aqueous humour at the ciliary body and its drainage at the angle of the eye; and the buoyancy-driven flow. Assuming the height of the anterior chamber in the anterior–posterior direction to be much less than its width, the governing equations of mass, momentum and energy conservation can be greatly simplified so that the solution may be found analytically. They also used the model to consider transport of particles, such as blood cells and pigment particles within the anterior chamber. Their model was extended by Fitt & Gonzalez (2006) to include also the possible buoyancy driven flow when the subject is supine, flows driven by vibrations of the natural lens and flows driven by the rapid eye movement during sleep, all of which models made use of lubrication theory.

A numerical model of the flow of aqueous humour in a smoothed, but otherwise realistic, geometry of the anterior chamber was developed by Heys *et al.* (2001) in which the iris was treated as an elastic solid, necessitating the solution of a fluid–structure interaction problem. This model was extended by Heys & Barocas (2002b) and Huang & Barocas (2006) to include models of accommodation of the lens, by Heys & Barocas (2002a) to including particle transport and an explanation of the formation of the condition known as Krukenberg's spindle, by Huang & Barocas (2004) to include active mechanics of the iris muscle, by Amini & Barocas (2010) to include the effect of corneal indentation, by Amini *et al.* (2012) to include the effect of the force on the cornea due to blinking, by Jouzdani *et al.* (2013) to include the effects of miosis (accommodation by the iris when the amount of light entering the pupil decreases). Abouali *et al.* (2012) also developed a numerical model of the flow in the anterior chamber, but assumed a rigid iris and focussed on the flow driven by saccades (rotations) of the eye.

To our knowledge there are few studies of flow in the presence of an implanted iris-fixated pIOL. Kawamorita *et al.* (2012) considered the effect of a sulcus-supported lens on the flow in the posterior and anterior chambers, although they did not account for the effect of thermal gradients, saccades or accommodation of the lens or iris. Niazi *et al.* (2012) and Repetto *et al.* (2015) performed numerical simulations of the flow in the presence of an implanted iris-fixated pIOL, looking in particular at the effects of the flow on the fluid shear stress experienced by the endothelial cells that line the posterior surface of the cornea and the pigment cells on the iris. Niazi *et al.* (2012) considered an idealized approximation of the realistic geometry and applied fixed temperature boundary conditions on the surfaces of the anterior chamber except for the posterior surface of the cornea. To set the temperature at the cornea they assumed a prescribed ambient temperature and set a convection condition at the outer surface of the cornea. They concluded that the presence of the lens decreases the typical velocity of the aqueous humour by around 35% and that the thermal properties of the device affect the flow significantly. Repetto *et al.* (2015) performed a similar investigation, but they did not account for the thermal properties of the device. However, as well as the buoyancy driven flow, they also considered the flow due to the production and drainage of aqueous humour, the flow produced by miosis (dilation/contraction of the pupil) and the flow induced by saccades (movements) of the eyeball.

In this article, we develop and solve a model of the dynamics of aqueous humour in the anterior chamber of the eye in the presence of a pIOL. We start by considering a toy model, which is a stripped down version of the realistic problem. We can find exact solutions of this model, and these allow us to

investigate the effect of the key parameters in the problem. We then consider the realistic problem, but with a slightly simplified geometry, and we provide a semi-analytic solution for the flow and pressure fields. The novelty of this work includes the use of a semi-analytic solution and the coupling of the thermal flow and the flow induced by aqueous production and drainage. Moreover, the semi-analytic solution enables us to access regimes that numerical solutions cannot, and, since the programs run quicker, we can more easily investigate the role of each parameter involved in the solution than with a fully numerical approach. Finally, the use of the present approach and the preliminary analysis on the toy model allows us to obtain better insight on the basic physical mechanisms underlying flow characteristics.

2. A toy model of the buoyancy driven flow

Before considering the flow generated in the anterior chamber of the eye in the presence of a pIOL, it is conceptually instructive to consider a simplified 2D model representing aspects of the real situation in the anterior chamber, and which also gives insight into the buoyancy-driven flow with the pIOL present.

We assume the flow is steady and 2D in the (x, z)-plane (ignoring the lateral direction) and that gravity acts parallel to the superior–inferior direction, modelling an upright person. We model both the anterior chamber and the region posterior to the pIOL as rectangles that are wide in the superior–inferior direction compared to the width of the anterior chamber in the anterior–posterior direction, see Fig. 2. We neglect the flow due to the production and drainage of aqueous humour, so that the domain is closed. We treat the aqueous humour as a Newtonian fluid with density ρ, constant shear viscosity μ and thermal conductivity k_a, and, employing the Boussinesq approximation, we assume the density in the gravitational acceleration

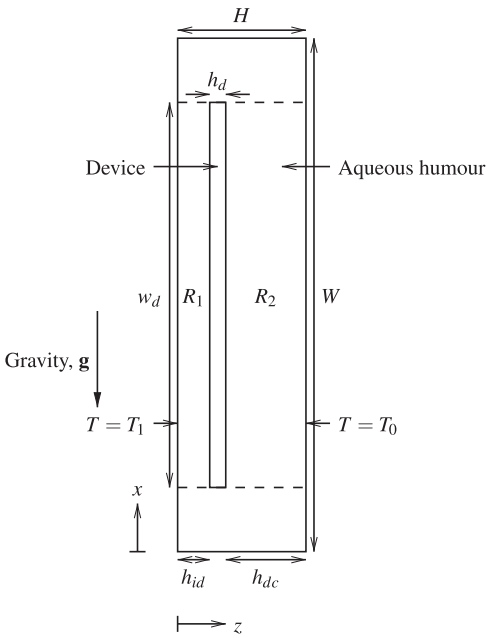

FIG. 2. Sketch of the simple conceptual model of buoyancy driven flow in the presence of a pIOL. Region R_1 is on the posterior side and R_2 is at the anterior, with the dashed lines indicating the ends of these regions.

term in the momentum equation is given by

$$\rho = \rho_0 \left(1 - \alpha_a \left(T - T_0\right)\right), \tag{2.1}$$

where T is temperature, ρ_0 is the density at the temperature $T = T_0$, which is used as a reference temperature, and α_a is the coefficient of thermal expansion, whilst the density is approximated as ρ_0 in the other terms in the governing equations. Finally, we model the device as a rigid solid with thermal conductivity k_d.

We assume that the surface $z = 0$, which represents the lens–iris is at a uniform temperature T_1 (approximately equal to body temperature) and that the surface $z = H$ representing the cornea is also at a uniform temperature T_0 (which depends on the ambient temperature) with $\Delta T = T_1 - T_0$.

Assuming regions R_1 and R_2 are sufficiently long and thin, we may neglect end effects in both regions, so that the velocity and temperature fields are fully developed (independent of x), and thus depend on z only. Solving the continuity equation then implies that the velocity field has only one component: $\mathbf{u} = u(z)\hat{\mathbf{x}}$. The z-component of the momentum equation can be solved to show that the pressure is independent of z, while the other components of the momentum equation and the energy equation respectively become (Canning *et al.*, 2002)

$$\nabla_h p = \mu \frac{\partial^2 \mathbf{u}_h}{\partial z^2} + \rho_0 \left(1 - \alpha_a \left(T - T_0\right)\right) \mathbf{g}, \qquad 0 = \frac{\partial^2 T}{\partial z^2}, \tag{2.2}$$

where p denotes mechanical pressure, and the subscript 'h' indicates the projection into the (x, y)-plane (although we only consider 2D flows in this section, we report the 3D lubrication equations, because they will be required in the next section). At the boundaries of the device, we apply no slip fluid velocity ($\mathbf{u} = \mathbf{0}$) and also continuity of temperature (T) and of normal heat flux ($-k\,\partial T/\partial z$).

With these assumptions, we can solve the governing equations analytically to show that the temperature has a piecewise linear profile:

$$T = \begin{cases} T_1 - \Delta T \dfrac{k_d z}{k_d(h_{id} + h_{dc}) + k_a h_d} & \text{in } R_1, \\ T_0 + \Delta T \dfrac{k_d h_{dc} + k_a(h_{id} + h_d - z)}{k_d(h_{id} + h_{dc}) + k_a h_d} & \text{in the device (for } k_d \neq 0), \\ T_0 + \Delta T \dfrac{k_d(H - z)}{k_d(h_{id} + h_{dc}) + k_a h_d} & \text{in } R_2, \end{cases} \tag{2.3}$$

(with T undefined in the device if $k_d = 0$), where z is the distance from the lens–iris surface (see Fig. 2). Since the right-hand side of (2.2) is independent of x, $\partial p/\partial x$ must be constant in R_1 and also in R_2, and matching with the pressures in the two rectangular end regions implies that the two constants are equal. Imposing equal and opposite fluxes in R_1 and R_2 for mass conservation leads to an equation that can be solved to give

$$\frac{dp}{dx} = \rho_0 g - \frac{\rho_0 g \alpha_a \Delta T (k_d(h_{id}^4 + 2h_{id}^3 h_{dc} + h_{dc}^4) + 2k_a h_d h_{id}^3)}{2(h_{id}^3 + h_{dc}^3)(k_d h_{id} + k_d h_{dc} + k_a h_d)}; \tag{2.4}$$

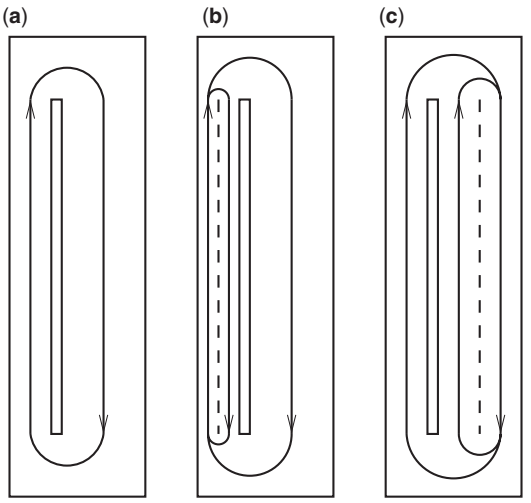

FIG. 3. Schematic diagram showing the three possible flow scenarios (a), (b) and (c). The dashed line shows stationary fluid, and the solid lines with arrows indicate the flow. The scenario that would be realized depends on the relative sizes of the lengths h_{id} and h_{dc}, see inequalities (2.7) and (2.8).

in regions R_1 and R_2, where g is the acceleration due to gravity (note that since the system is enclosed, the pressure must be specified somewhere to find its absolute value). The velocity in R_1 is

$$u = \frac{\rho_0 g \alpha_a \Delta T}{12\mu(h_{id}^3 + h_{dc}^3)(k_d(h_{id} + h_{dc}) + k_a h_d)} \times \left(2k_d(h_{id}^3 + h_{dc}^3)z - k_d(3h_{dc}^4 + 4h_{id}h_{dc}^3 + h_{id}^4) - 6k_a h_d h_{dc}^3\right) z(h_{id} - z), \tag{2.5}$$

and in R_2 it is

$$u = \frac{\rho_0 g \alpha_a \Delta T}{12\mu(h_{id}^3 + h_{dc}^3)(k_d(h_{id} + h_{dc}) + k_a h_d)} \times \left[k_d(h_{id}^4 - 2h_d h_{id}^3 - 2h_d h_{dc}^3 - h_{dc}^4 - 2h_{id}h_{dc}^3 + 2h_{id}^3 h_{dc}) + 6k_a h_d h_{id}^3 + 2k_d(h_{id}^3 + h_{dc}^3)z\right] \times (H - z)(z - h_{id} - h_d). \tag{2.6}$$

It can be shown that there are three qualitatively different possible velocity fields, and these are illustrated in Fig. 3. In scenario (a) the flow is unidirectional both anterior to and posterior to the pIOL, whilst in (b), there is flow reversal and an extra circulation posterior to the pIOL, and in (c) there is flow reversal anterior to the pIOL. Note that the existence of an extra circulation implies a qualitatively different flow; in particular the direction of the shear stress on the wall next to the extra circulation is reversed. Scenario (b) occurs whenever

$$6(1 + c)l^3 - 6l^2 + 4l - 1 < 0, \tag{2.7}$$

where $l = h_{dc}/(h_{id} + h_{dc})$ and $c = (k_a h_d)/(k_d(h_{id} + h_{dc}))$, and scenario (c) occurs when

$$6(1 + c)l'^3 - 6l'^2 + 4l' - 1 < 0, \tag{2.8}$$

where $l' = h_{id}/(h_{id} + h_{dc}) = 1 - l$, and if neither of these two inequalities hold then scenario (a) occurs (both inequalities cannot hold simultaneously).

Inspection of the above inequalities shows that, if $k_d = 0$, i.e. in the case of a thermally insulating pIOL, then only scenario (a) is possible. For any finite choice of the thermal conductivities k_a and k_d, scenario (a) occurs if h_{dc} is less than a critical value, whilst scenario (c) occurs if h_{id} is sufficiently small. Since the lens is typically placed nearer to the lens–iris than to the cornea, only scenarios (a) and (c) are expected to be possible in reality. In addition, if k_d is small compared to k_a, then h_{id} is restricted to very small values for scenario (c) to occur. Since the thermal conductivity of the aqueous is typically significantly larger than that of the pIOL, we are likely only to observe scenario (a) in reality. Furthermore, the realistic situation is more complicated than this toy model; in particular, the presence of the pIOL can generate 3D flows, as will be seen in the following sections.

3. Model of flow in the anterior chamber with a pIOL

In this section, we develop a mathematical model to find the flow of aqueous humour in the anterior chamber in the presence of a pIOL. We model the anterior chamber as axisymmetric, as small variations from this geometry are not expected to affect the flow significantly. We assume that gravity acts parallel to the superior–inferior direction (i.e. perpendicular to the axis of symmetry), modelling an upright person. As in Section 2, we assume steady flow, assume that the geometry is much shorter in the anterior–posterior direction than the superior–inferior and lateral directions, treat the aqueous humour as an incompressible Newtonian fluid with constant viscosity, and use the Boussinesq approximation (2.1) to account for density variations. In order use of the lubrication equations (2.2) we also need to assume that the reduced Reynolds number and the Prandtl number multiplied by the reduced Reynolds number are both small, and we justify this in Section 4.1. As in Section 2 we set fixed temperature boundary conditions on the interior surfaces of the anterior chamber, and we use the same symbols to denote the fluid and pIOL properties.

The model geometry is shown in Fig. 4. We work in Cartesian coordinates (x, y, z) and cylindrical polars (r, θ, z) interchangeably, where in both coordinates z is in the anterior–posterior direction and the $+x$-direction corresponds to $\theta = 0$, and we denote the pupil radius r_p, the pIOL radius r_d and the anterior chamber radius r_{ac} (with $r_{ac} > r_d > r_p$). We denote the anterior surface of the natural lens $z = z_l(r)$, the anterior surface of the iris $z = z_i(r)$, the posterior and anterior surfaces of the device $z = z_{dp}(r)$ and $z = z_{da}(r)$, respectively, and the posterior surface of the cornea $z = z_c(r)$. We assume that gravity acts in the $+x$-direction with magnitude g and acceleration vector $\mathbf{g}$ (note that if the gravitational vector were not perpendicular to z the only difference would be that a hydrostatic pressure gradient would be set up, and the gravitational acceleration g would appear multiplied by the sine of the angle from the z-direction).

We assume the anterior surfaces of the lens and iris are maintained at the constant temperature $T = T_1$ (body temperature), and the the posterior surface of the cornea is at the reference temperature $T = T_0$.

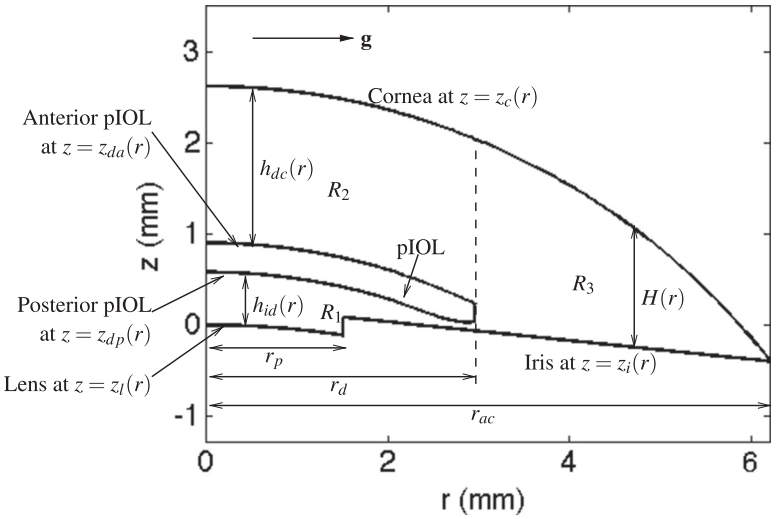

FIG. 4. Cross-section of the plane $\theta = 0$, showing the model anterior chamber lens, iris, cornea and device and acceleration due to gravity $\mathbf{g}$. The 3D geometry is found by rotating through all angles $0 \leq \theta < 2\pi$ about the axis $r = 0$. The key lengths are shown, as well as the regions R_1, R_2 and R_3 in which the flow is calculated. In this diagram h_{id} denotes the height of the region posterior to the pIOL ($h_{id} = z_{dp} - z_l$ in $0 < r < r_p$ and $h_{id} = z_{dp} - z_i$ in $r_p < r < r_d$), h_{dc} is the height of the region anterior to the pIOL ($h_{dc} = z_c - z_{da}$ in $r < r_d$) and H is the height of the anterior chamber ($H = z_c - z_i$ in $r_d < r < r_{ac}$). Note that the orientation is rotated through 90° from that in Fig. 1.

4. Solution

4.1 *Discussion of modelling assumptions*

In this section we discuss the validity of the modelling assumptions that we have applied. Figure 5 gives the model dimensions that have been used and Table 1 lists the non-geometrical parameters that will be used for the estimates in this section. We were unable to find a value for the thermal conductivity of the device, k_d. We will focus on the representative values $k_d = 0$ in Sections 5.1 and 5.3 and $k_d = k_a$ in Section 5.4, as well as discussing the effect of this parameter value more generally in Section 5.4.

The fixed-temperature condition at the cornea might not be realistic, because in reality the external atmospheric temperature would be fixed, meaning that applying Newton's law of cooling plus an evaporation condition at the anterior surface of the cornea would be more realistic. However, Efron *et al.* (1989) found that the maximum temperature difference between central and peripheral cornea is only about 0.5°C, and moreover Heys & Barocas (2002a) pointed out that there are no suitable estimates of the heat transfer coefficient. Instead in their work they set the temperature on the external surface of the cornea and solved for the temperature distribution within the cornea to find the heat flux through it, and this was applied as a boundary condition on the internal surface; their results show that the temperature on the internal surface is fairly uniform over the majority of that surface. For simplicity in this article and to reduce the number of unknown parameters, we set the posterior corneal surface temperature, although it is straightforward to extend the model and use a more sophisticated boundary condition. At the lens and iris we set the temperature equal to body temperature, following Heys & Barocas (2002a).

In the model we use lubrication theory to simplify the equations, and so here we check the validity of its assumptions. The short lengthscale is the width of the chamber in the anterior–posterior

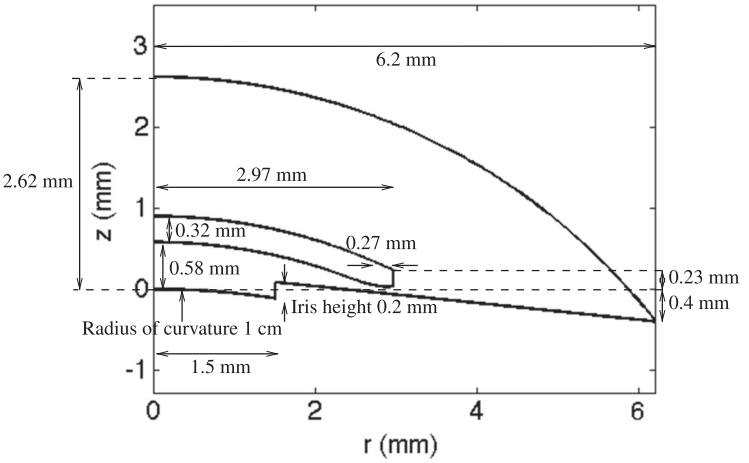

FIG. 5. Labelled diagram showing the lengths parameterizing the geometry. The lens, cornea and anterior of the pIOL are modelled as arcs of circles, and the iris is treated as a straight line. The posterior surface of the pIOL is a circular arc with the same radius as the anterior, but displaced by 0.32 mm, except in the outer 0.27 mm of the pIOL, where it is modelled as a line. Smoothing is applied over a region of width 0.4 mm centred on the point of discontinuity of gradient (i.e. in the region 2.5 mm $\leq r \leq$ 2.9 mm) by fitting a cubic polynomial such that the function describing the posterior of the device is everywhere C^1. This geometry is based on the Artiflex lens and was provided by Ophtec.

TABLE 1 *Non-geometrical parameter values used in the model. *The temperature T_0 was estimated using a CFD model of the eye, ignoring fluid flow.*

Symbol	Description	Value	Reference
Q	Total aqueous flow through eye	3 μl/min or 5×10^{-11} m^3/s	Brubaker (1989, 1991)
T_1	Body temperature	37°C	
T_0	Temperature on posterior cornea	34°C	*
ρ_0	Density of aqueous at T_0	1000 kg/m^3	
ν_a	Kinematic viscosity of aqueous humour at 37°C	7.5×10^{-7}	Beswick & McCulloch (1956)
k_a	Thermal conductivity of aqueous	0.578 W/m/K	Poppendiek *et al.* (1967)
α_a	Thermal expansion coefficient of aqueous (use water at 30°C)	3×10^{-4} /K	Batchelor (1967)
g	Acceleration due to gravity	9.81 m/s^2	

direction, and we use the representative length $h_{dc} = 1.72$ mm, whilst for the long lengthscale we use $2r_{ac} = 12.4$ mm, which means the ratio of lengthscales is $\epsilon \approx 0.14$. We use the velocity scale $U = 0.5$ mm/s (estimated *a posteriori* from our results), which leads to the reduced Reynolds

TABLE 2 *Table showing values parameterizing the temperature profile in the three regions, where* $\Delta T = T_1 - T_0$.

Region	R_1 $0 \le r \le r_d$	R_2 $0 \le r \le r_d$	R_3 $r_d \le r \le r_{ac}$
z_{lo}	z_l $(0 \le r \le r_p)$ or z_i $(r_p \le r \le r_d)$	z_{da}	z_i
z_{up}	z_{dp}	z_c	z_c
z_p	z_l $(0 \le r \le r_p)$ or z_i $(r_p \le r \le r_d)$	z_c	z_c
T_p	T_1	T_0	T_0
G	$\frac{-\Delta T k_d}{k_d(h_{id}+h_{dc})+k_a h_d}$		$\frac{-\Delta T}{H}$

number

$$Re_{\text{red}} = \epsilon^2 \frac{U(2r_{ac})}{\nu} \approx 0.016, \tag{4.1}$$

whilst the Prandtl number $\sigma = \rho c_p \nu_a / k_a \approx 5.4$. Thus the assumptions of lubrication theory hold, that is ϵ, Re_{red} and σRe_{red} are all small, and so the flow and temperature fields are to a good approximation governed by (2.2).

4.2 *Solutions for the pressure and flow*

We define three regions of the anterior chamber: R_1 posterior to the device $(0 \le r \le r_d)$, R_2 anterior to the device $(0 \le r \le r_d)$ and R_3 being the outer region given by $r_d \le r \le r_{ac}$, and these are illustrated in Fig. 4. As with the toy model, solving (2.2b) gives a piecewise linear temperature profile:

$$T = T_p + G\big(z - z_p\big), \tag{4.2}$$

where $T = T_p$ at the specified point $z = z_p$ (given by a boundary condition), with the gradient G (which is independent of z) set by the relative thermal diffusivities and the height of the chamber, and reported in Table 2.

Solving (2.2a) shows that the (r, θ)-components of the velocity field depend upon the unknown gradients of the pressure field with a cubic dependence on z as follows:

$$\mathbf{u}_h = -\frac{1}{2\mu}\left[\nabla_h p - \rho_0 \mathbf{g}\left(1 - \frac{\alpha_a G}{3}\left(z + z_{up} + z_{lo} - 3z_p - \frac{3(T_0 - T_p)}{G}\right)\right)\right](z - z_{lo})\big(z_{up} - z\big), \tag{4.3}$$

where the chamber spans the range $z_{lo} \le z \le z_{up}$. The z-integrated velocity has simpler expression:

$$\mathbf{q}_h = \int_{z_{lo}}^{z_{up}} \mathbf{u}_h \, dz = -\frac{h^3}{12\mu}\left(\nabla_h p - \rho_{\text{mid}} \mathbf{g}\right), \tag{4.4}$$

where $h = z_{up} - z_{lo}$ is the height of the chamber (in the z-direction) and ρ_{mid} is the density at the midpoint $z = (z_{lo} + z_{up})/2$, and applying mass conservation $(\nabla_h \cdot \mathbf{q}_h = 0)$ shows that the pressure can be decomposed

as the sum of two terms:

$$p = p_0(r) + p_1(r)\cos\theta, \tag{4.5}$$

where θ is the angle from the x-axis (the downwards direction), satisfying

$$\frac{1}{r}\frac{d}{dr}\left(rh^3\frac{dp_0}{dr}\right) = 0, \tag{4.6}$$

$$\frac{1}{r}\frac{d}{dr}\left(rh^3\frac{dp_1}{dr}\right) - \frac{h^3 p_1}{r^2} = g\frac{d}{dr}\left(h^3\rho_{\text{mid}}\right). \tag{4.7}$$

Correspondingly,

$$\mathbf{q}_h = -\frac{h^3}{12\mu}\left\{\frac{dp_0}{dr}\hat{\mathbf{r}} + \frac{dp_1}{dr}\cos\theta\hat{\mathbf{r}} - \frac{p_1}{r}\sin\theta\hat{\boldsymbol{\theta}} - \rho_{\text{mid}}\mathbf{g}\right\}, \tag{4.8}$$

and imposing an axisymmetric radially outward flux F at $r = r_{ac}$ implies the boundary conditions

$$\frac{dp_0}{dr} = -\frac{12\mu F}{2\pi R h^3}, \tag{4.9}$$

$$\frac{dp_1}{dr} = \rho_{\text{mid}} g \tag{4.10}$$

at the outer edge of the anterior chamber, whilst imposing the axisymmetric pressure p_p at the edge of the pupil $r = r_p$ in Region 1 implies $p_0 = p_p$, $p_1 = 0$ there. Note that the edge of the pupil is also a source of fluid with total flux F, which need not be axisymetrically distributed. We also impose continuity of volumetric flux and continuity of pressure at $r = r_p$ posterior to the device and at $r = r_d$. Table 2 lists the values of the key geometrical parameters, T_p and the temperature gradient G in each of the regions of the model.

The flow driven by the component $p_0(r)$ of the pressure represents the axisymmetric, radially outward flow that is driven by the production of aqueous humour in the ciliary body and its drainage into Schlemm's canal and the aqueous veins, and thus if there is no such production and drainage we would have $p_0 = p_p$ everywhere. The flow driven by $p_1(r)\cos\theta$ arises due to the combined effects of gravity and density fluctuations due to the temperature profile. This decomposition of the flow field agrees with the findings of Canning *et al.* (2002) and Fitt & Gonzalez (2006), who considered a similar model with no implanted lens and a simpler geometry and found the flow corresponding to p_1. Note that when the eyelids are closed there would be almost no temperature variation at the boundaries, and the only flow would be due to the production/drainage.

5. Results

5.1 *Insulating device and no production or drainage of aqueous humour*

Initially, we assume the device is perfectly insulating and there is no production and drainage of the aqueous humour. This implies $p_0 = p_p$ everywhere, and thus we focus only on the solution for p_1 and the resulting thermally driven flow.

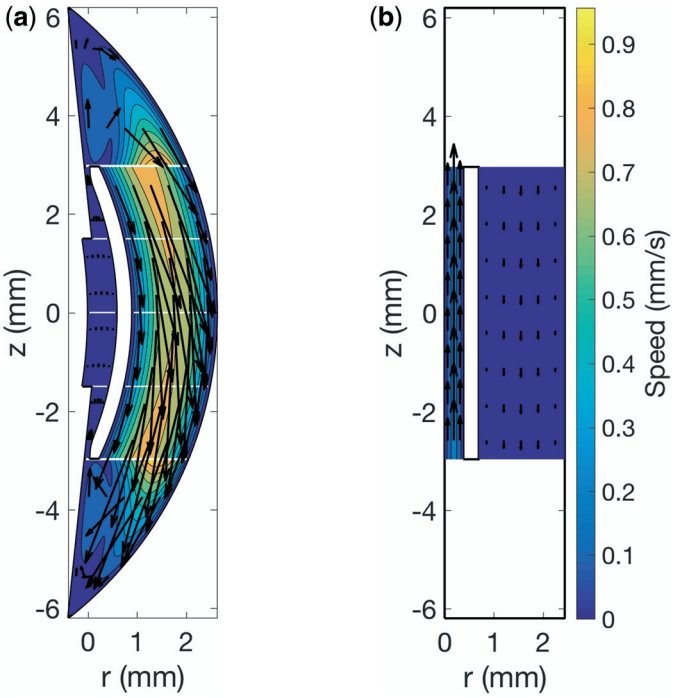

FIG. 6. (a) Velocity vectors and velocity magnitude (shading) on the cross-section $\theta = 0, \pi$ of the anterior chamber (vertical plane) with no flow due to production and drainage of aqueous. (b) Velocity vectors and magnitude in the toy model, with the heights H, h_d, h_{id}, h_{dc} chosen so that the areas of R_1, R_2 and the device in part (b) are respectively equal to the areas posterior to the pIOL, anterior to the pIOL and of the device in part (a). For both diagrams the device is thermally insulating, $k_d = 0$, and the scaling of the velocity vectors and the shading is the same.

Contours of the velocity magnitude and superposed velocity vectors on the cross-section that is the vertical symmetry plane are shown in Fig. 6(a). The flow on this plane consists of a single circulation cell, with fluid particles moving downwards anterior to the pIOL and upwards posterior to it. The flow predicted by the toy model of Section 2, which is given by (2.5) and (2.6), is shown in Fig. 6(b) for comparison. In the case of an insulating device, the toy model predicts that scenario (a) will occur (see Fig. 3), and the predicted directions of the flow are the same in the 3D model. However, the magnitudes of the flow vectors are quite different in the two cases, as explained below.

Figure 7 shows the (r, θ)-components of the flow, and in panels (a), (b) and (c) we show the streamlines, which give the direction of the depth-averaged flow, and are colour-coded to indicate the volumetric flux between neighbouring streamlines; in panels (d), (e) and (f) we show the speed of the depth-averaged flow. In the figure the three circles represent the external boundary of the anterior chamber, the pIOL and the pupil, respectively. In the left column we report the solution anterior to the device, in the middle column the solution posterior to the pIOL and, finally, in the right column the solution external to the pIOL. These results show that the total buoyancy-driven flow constitutes a volume flux of about 300 μl/min (based on the spacing between the streamlines in Fig. 7(a)), which is larger than the flow due to the production/drainage of aqueous by a factor of around 100 (see Table 1).

The pressure is approximately hydrostatic, deviating by less than 0.01% from this value.

We note that the assumptions of lubrication theory do not hold at the following three discontinuities: the edge of the pupil $r = r_p$; the edge of the device $r = r_d$; and the edge of the anterior chamber $r = r_{ac}$ (see Fig. 4). This means that the details of the flow are likely to be inaccurate in the region near to these boundaries; in particular, although the model predicts large discontinuities in the velocity and other fields, the true velocity field is smooth.

The model predicts the fastest flows to be just outside the pIOL, see Fig. 7(f), and even though this is a region in which inaccuracies are expected, we anticipate the maximum will be close to this point since the result is so strong. The flow anterior to the device is approximately constant in both magnitude and direction, while the flow posterior to the device is very small indeed. The streamlines in the region external to the device are curved, indicating that the flow is highly 3D. In particular, fluid particles move downwards in front of the pIOL and then are drifted up along the sides of the anterior chamber. The results are in very good qualitative agreement with the fully numerical results obtained by Repetto *et al.* (2015) and Niazi *et al.* (2012). Comparing Fig. 7(d, f) with Fig. 8 of Repetto *et al.* (2015) shows that the lubrication approximation leads to significant overestimation of the velocity near the edges of the device, but otherwise provides a reliable estimate.

Inspection of the flow shown in Fig. 7 shows that most of the flow circulates around anterior to the device, with a strong downwards flow anterior to the device and the flow returning to the top in the extreme lateral regions. There is very little flow anterior to the device. In contrast in the toy model, there is no alternative lateral path for the fluid to return to the top, meaning that the resistance to flow is higher and the total volumetric flux lower.

It is also of interest to calculate the shear stress arising due to this flow, and its value on the different surfaces is shown in Fig. 8. In the figure the arrows indicate the direction of the stress. The maximum shear stress on the cornea is located close to the boundary of the pIOL and this is also in good agreement with the simulations of Repetto *et al.* (2015) shown in Fig. 9 of that article, except in the region just outside the device. Note that the stress, similarly to the velocity magnitude, is not continuous across the boundaries of the various regions, as a consequence of the lubrication theory approximations, but we expect the real solution to be smooth across these boundaries. We also observe that the wall shear stress on the cornea and on the anterior face of the pIOL have the same direction, indicating that a circulation does not form anterior to the pIOL. This agrees with the prediction of the toy model presented in Section 2.

5.2 *Comparison with the case of the natural eye*

We recall here the case with no pIOL present, which was studied by several authors, both analytically and numerically (Canning *et al.*, 2002; Heys & Barocas, 2002a). In this case, if the aqueous production/drainage flow is neglected, the flow takes place on vertical planes parallel to the axis of symmetry of the anterior chamber (Canning *et al.*, 2002). Thus the implantation of a pIOL significantly modifies the flow structure in the anterior chamber, being responsible for the three-dimensionality of the velocity field.

With no pIOL the depth-averaged flow equals zero but there is still a flux around the chamber. It is straightforward to find the volumetric flux circulating in the anterior chamber, which is given by

$$\frac{\rho_0 g \alpha \Delta T}{192 \mu} \int_0^{r_{ac}} h^3 \, dr, \tag{5.1}$$

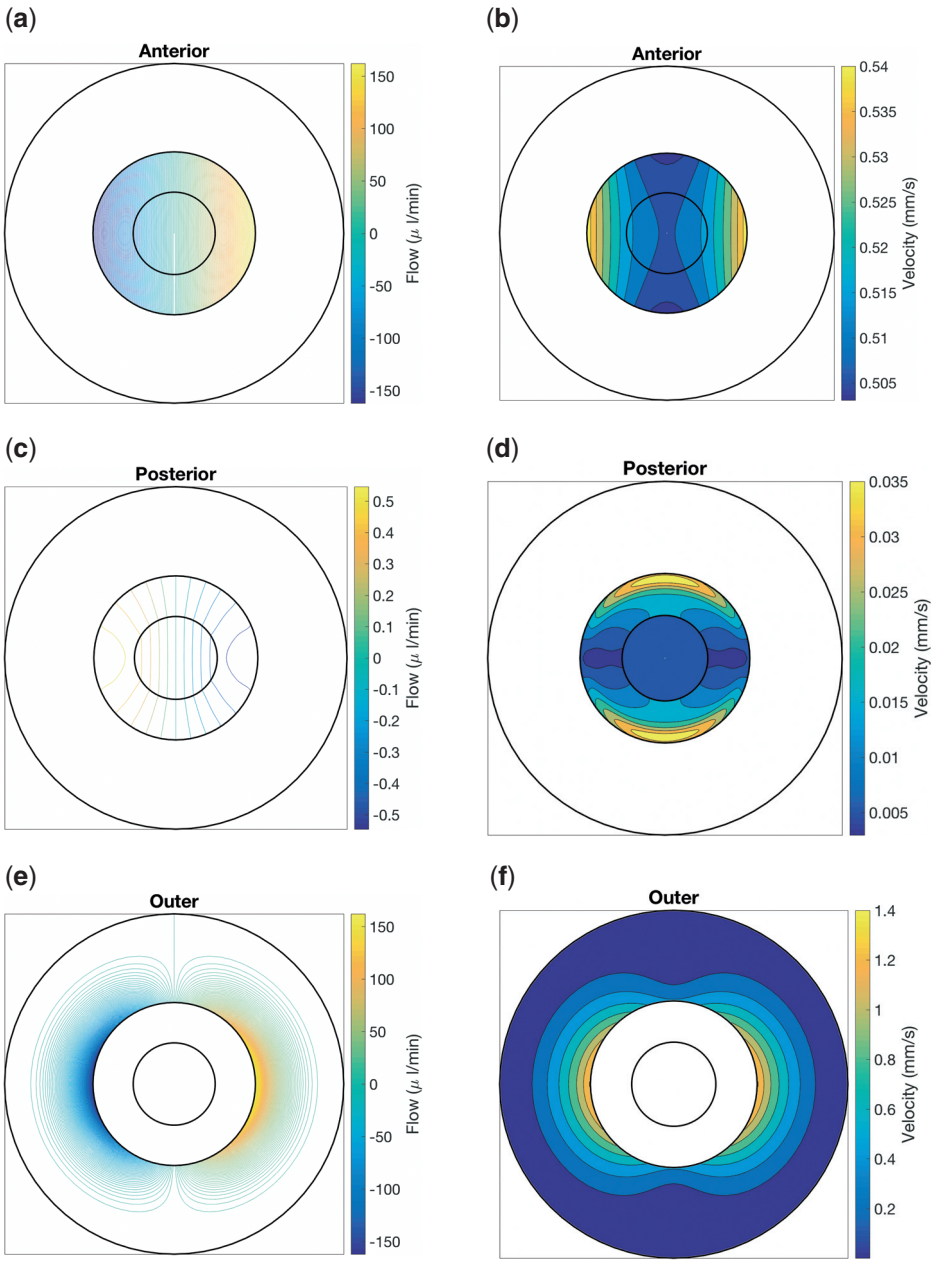

FIG. 7. Flows in the anterior chamber with a perfectly insulating device and no flow due to production/drainage of aqueous. (a), (b) Flow anterior to the device; (c), (d) flow posterior to the device; (e), (f) flow around the device in region R_3. Parts (a), (c), (e) show streamlines of the depth-averaged flow, which indicate the direction of flow, and the numerical scale quantifies the volumetric flux that occurs between neighbouring contour lines (contour lines spaced by 10 μl/min in (a) and (e) and by 0.1 μl/min in (c)). Parts (b), (d), (f) show the depth-averaged flow speed.

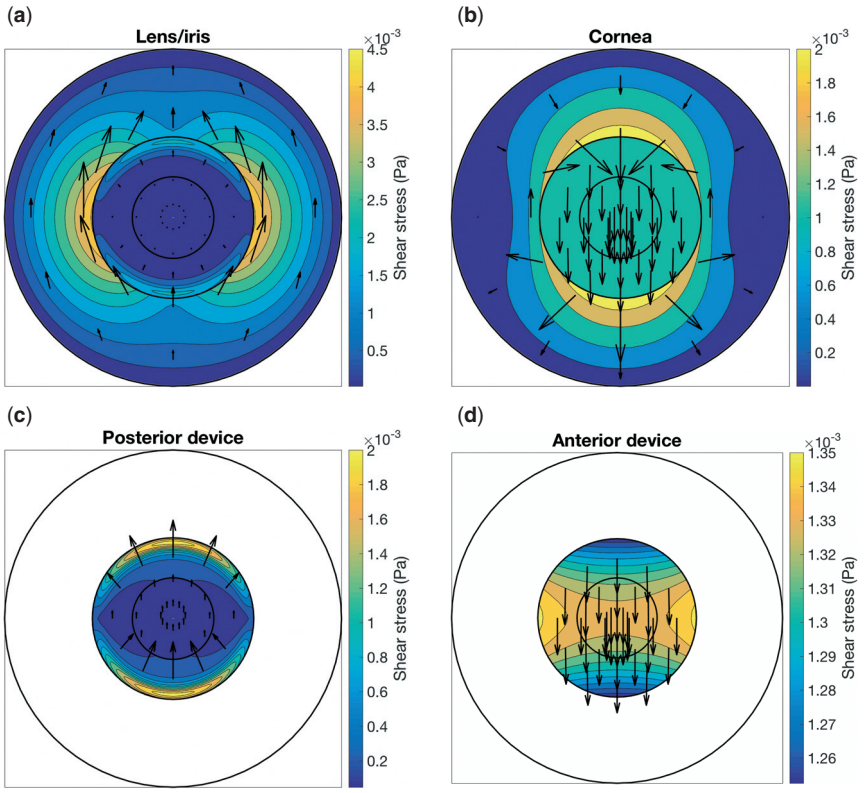

FIG. 8. Magnitude of the shear stress on the surfaces in the case with an insulating device and no flow due to production/drainage of aqueous with arrows to indicate the direction: (a) lens ($r < r_p$) and iris ($r_p < r < r_{ac}$), (b) cornea, (c) posterior surface of the implanted lens and (d) anterior surface of the implanted lens.

where h is the height of the anterior chamber, which equals about 200 μl/min. In turn this suggests that the presence of the device does not significantly affect the order of magnitude of the flow.

The shear stresses with no pIOL present are shown in Fig. 9 on the iris/lens and on the cornea, which are equal and opposite in this case. Comparing with Fig. 8 we can see that the maximum stress on the iris/lens is approximately doubled by the presence of the lens, whereas that on the cornea increases only very slightly in some regions (and is decreased in other places).

5.3 *Effect of the flow due to production/drainage of aqueous humour*

If the volumetric flux is set to a typical physiological value of $Q \approx 3$ μl/min then the flow due to buoyancy is much larger in magnitude than the flow due to the production and drainage of the aqueous humour (see Table 1). However, the flow arising from the production and drainage of the aqueous could make a significant difference in places where the geometry is constricted, and furthermore it is straightforward to include it. In this section we consider its effect. Solving for $p_0(r)$ as well as $p_1(r)$, we find that the radial flow component arising from the production and drainage of the aqueous only occurs in Regions R_2 posterior to the device and R_3. However, the total pressure is still dominated by the hydrostatic component.

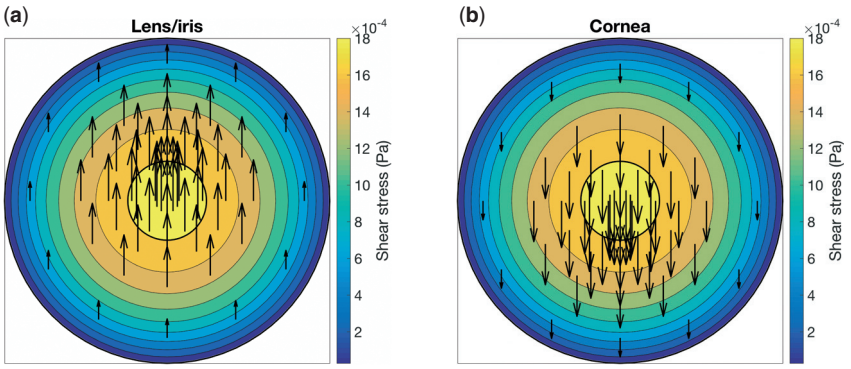

FIG. 9. Magnitude and directions of the shear stress on the surfaces, corresponding to the geometry shown in Fig. 5 but with no device present: (a) lens ($r < r_p$) and iris ($r_p < r < r_{ac}$), (b) cornea.

Close inspection of the pressure profile shows the biggest deviations from the hydrostatic profile occur in the narrow gap between the pIOL and the iris.

The change in the axisymmetric component of the pressure across a narrow gap is given by

$$\Delta p_0 = \frac{6\mu Q}{\pi} \int_{r_1}^{r_2} \frac{dr}{rh^3}, \tag{5.2}$$

where $h(r)$ is the (small) height of the region and Q is the volumetric flow rate. Adopting the typical parameter values listed in Table 1 we can get an estimate of the pressure drop across the constriction. A gap of 0.1 mm corresponds to a pressure drop of around 10^{-4} mmHg, and a gap of height around 0.01 mm that are sustained for a substantial fraction of a mm could affect the pressure by up to about 0.1 mmHg. Thus the pressure increase induced by a pIOL correctly positioned is tiny compared to the IOP ($\approx$ 15 mmHg) and does not have clinical significance.

The thermal flows with the addition of the flow induced by aqueous production/drainage are shown in Fig. 10, and, comparing with the case with no production or drainage of aqueous shown in Fig. 7, we observe that the flow due to production/drainage only makes a significant difference in the region between the iris and the device (see Fig. 10(d) for example).

The corresponding shear stresses are shown in Fig. 11, and, comparing with Fig. 8, we can see that there are significant differences on the iris and the device in the region where these two are close, especially in the top part of the eye. However, there is no change to the order of magnitude of either the flow or the shear stress, and we therefore conclude that, in the absence of incorrect positioning of the lens or other pathology of or insult to the eye, the differences are not significant enough to lead to damage.

5.4 *Effect of the thermal properties of the device*

So far we have assumed the device is perfectly insulating, but in reality this is not the case, and we investigate the effect of the thermal conductivity of the device in this section. In Fig. 12 we show the dependence of the flow against the value of the thermal conductivity of the device. We use the maximum shear stress to quantify the flow as this acts as a measure of the flow strength. As the graph shows, there is a significant dependence of the flow on the thermal properties.

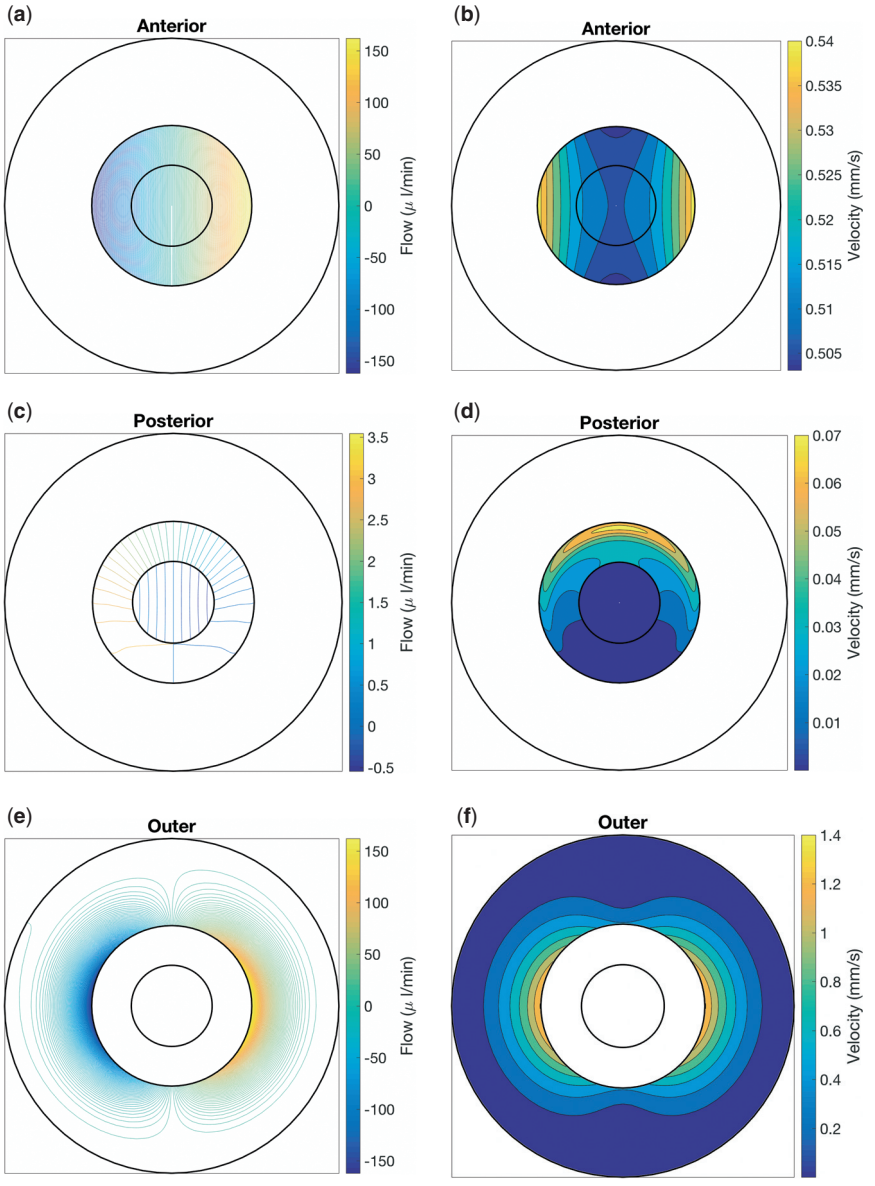

FIG. 10. As for Fig. 7 but including flow due to production/drainage of aqueous.

In what follows, we show results for the case in which the implanted device has thermal conductivity k_d equal to that of the aqueous humour k_a. Moreover, we also include the flow due to production and drainage of aqueous humour in these calculations, but as before this only makes a discernible difference in the region between the device and the iris. Contours of the velocity magnitude and velocity vectors are presented in Fig. 13(a) on the vertical plane of symmetry. In this case there is circulation anterior to the

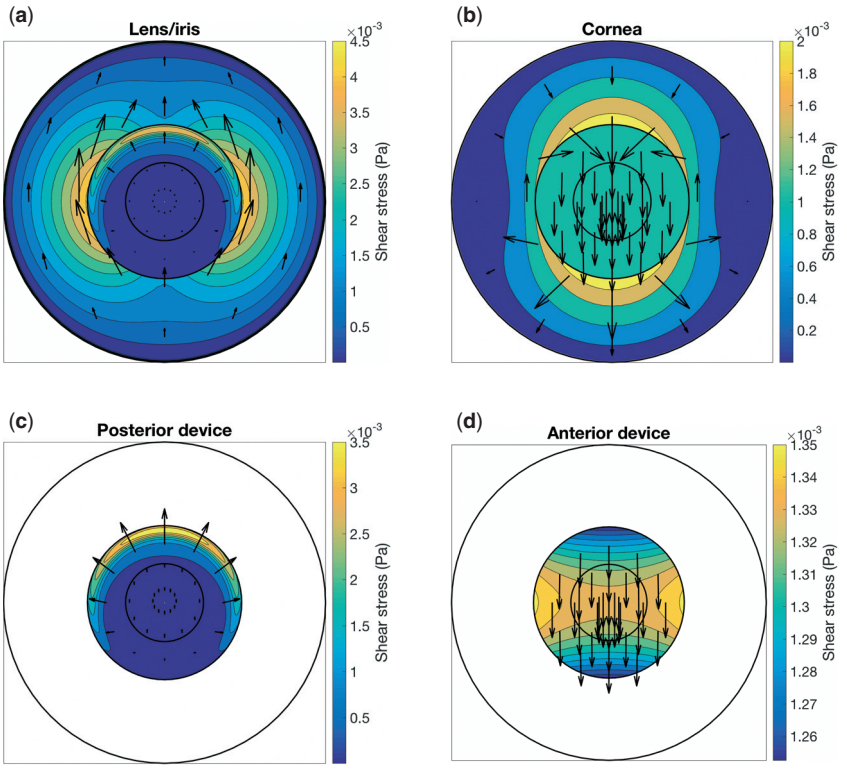

FIG. 11. As for Fig. 8 but including flow due to production/drainage of aqueous.

device as well as the circulation around the device, which is similar to scenario (c) in Fig. 3, and in this case too the toy model predicts the same qualitative flow, see Fig. 13(b).

Figures 14 and 15 show the flow and shear stress for this case. As can be seen by comparing with Figs 10 and 11, the thermal conductivity makes a more significant difference to the results. Although the flow goes in much the same directions in both cases, the total volumetric flux drops by a factor of about four from 300 μl/min to less than 80 μl/min in the case with heat conduction (Figs 10(c) and 14(c)), and the depth-averaged flow speeds are also significantly reduced, especially anterior to and outside of the device. On the other hand, the shear stresses have similar sizes for the case with and without thermal conduction included, although the distributions are different. In turn this means that the regions exposed to the highest stresses are different. The shear stress remains low on all surfaces, with the maximal value being around 4×10^{-3} Pa, which is attained on the iris under the top of the rim of the device. Also notice that the shear stress on the anterior of the device is predominantly upwards, agreeing with the qualitative prediction of the toy model, and in contrast to the flow with a thermally insulating device.

6. Discussion

We have developed a theoretical model to estimate the flow and shear stress in the anterior chamber with and without an iris-fixated pIOL present. The main assumption underlying the model is that each region in which the domain is subdivided is thin in one direction and wide in the other two orthogonal directions.

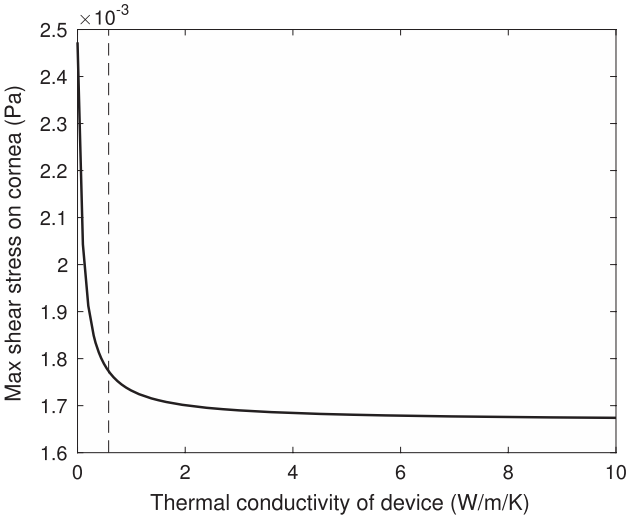

FIG. 12. Graph of the maximum shear stress on the cornea against the thermal conductivity of the device. Dashed line shows the value of the thermal conductivity of the aqueous 0.578 W/m/K (which was used as a value for k_d in Section 5.4).

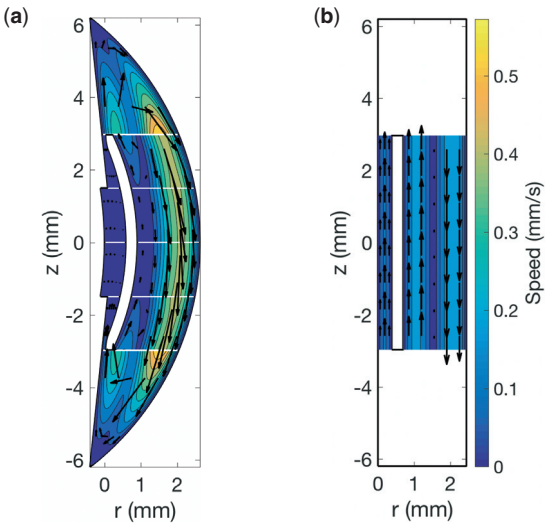

FIG. 13. As for Fig. 6, but with flow due to production and drainage of aqueous included in (a) and for a device with thermal conductivity $k_d = k_a$. The scale of the vectors and shading is the same in both plots.

Under these assumptions and making use of the lubrication theory we solve the equations in a semi-analytical way. We considered both the flow induced by aqueous production/drainage and the thermal flow produced by temperature variations across the anterior chamber. A similar problem has been studied with fully numerical approach by Niazi *et al.* (2012) and Repetto *et al.* (2015). In Niazi *et al.* (2012) only the thermally driven flow was considered, whereas Repetto *et al.* (2015) considered various mechanisms that generate fluid flow in the anterior chamber but neglected the effect of heat transport across the

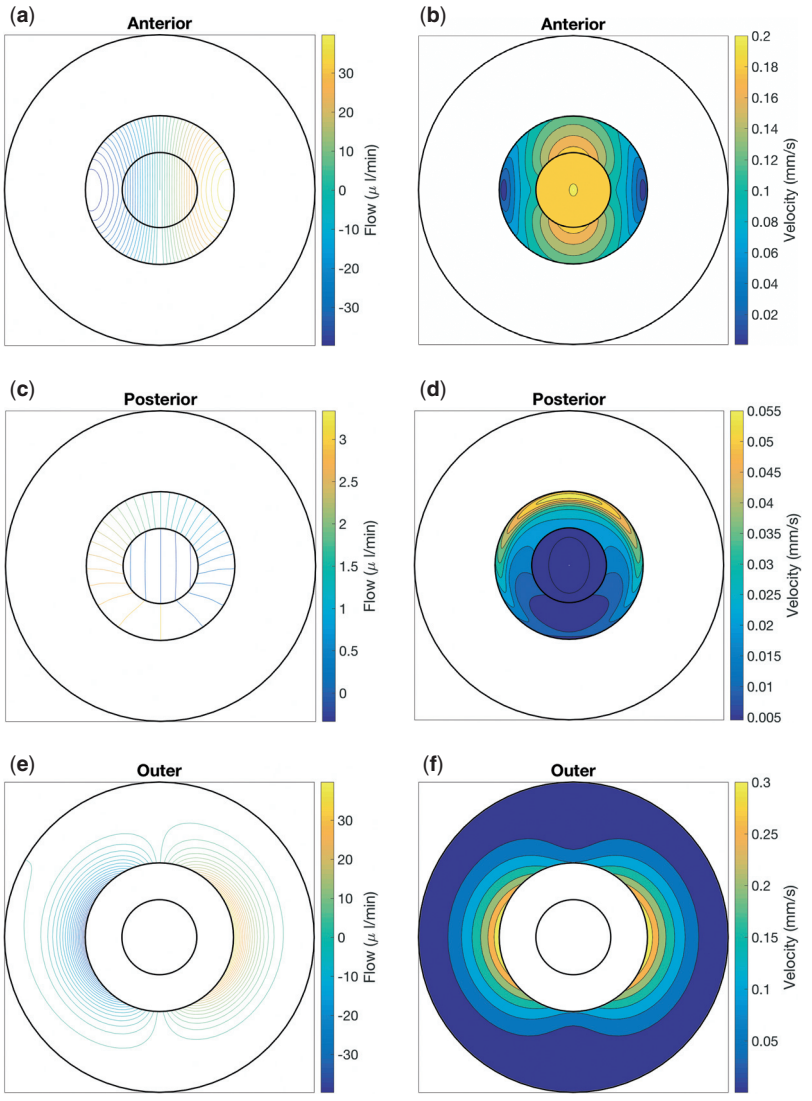

FIG. 14. As for Fig. 7 but including flow due to production/drainage of aqueous and heat conduction in the device with the device conductivity equal to that of the aqueous humour.

pIOL. We note that an analytical approach, even if it is based on the solution of a simplified version of the governing equations, also has some advantages over a fully numerical approach. In particular, the solution is found for all parameter values, leading to a better understanding of the behaviour of the system. This allows us to study how the solution depends on controlling parameters effectively. Before discussing the flow in a realistic geometry we also have considered a simple, highly idealized model of a unidirectional thermally driven flow, which, in our view, helps improving our understanding of the solution in the real case.

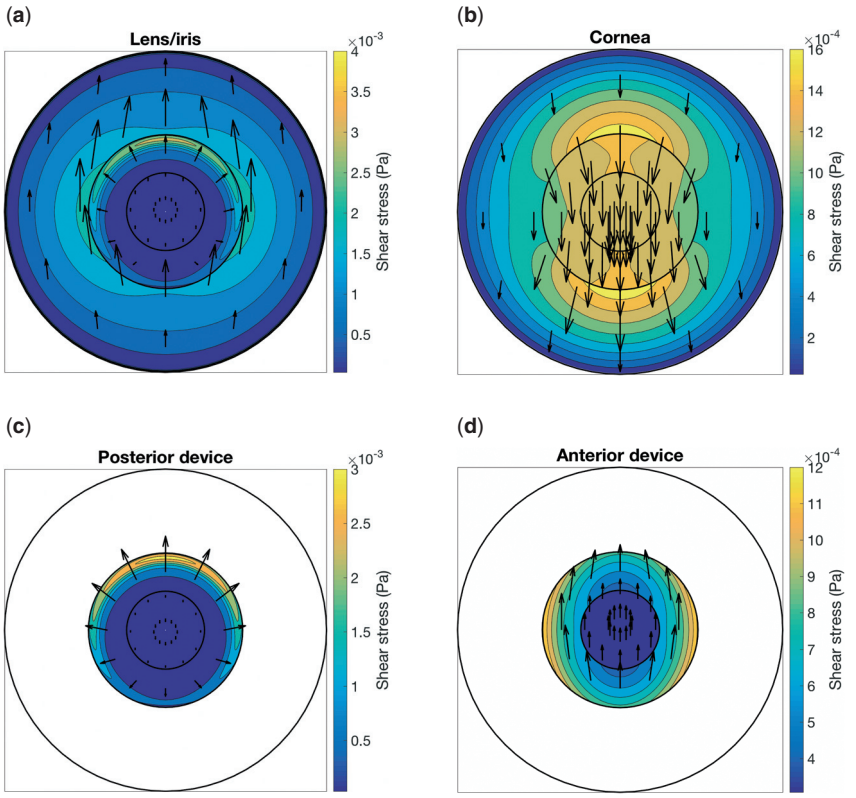

FIG. 15. As for Fig. 8 but including flow due to production/drainage of aqueous and heat conduction in the device with the device conductivity equal to that of the aqueous humour.

In the model we assumed that the viscosity of the aqueous humour is independent of temperature (this assumption was also made in all previous studies). In reality the viscosity varies significantly with temperature, and in fact the variation is much more than that of the density (whose effect we do include according to the Boussinesq approximation). Over the 3°C temperature variation considered here, the viscosity varies by about 6% of its value (Kestin *et al.*, 1978), while the density varies by only about 0.1%. Nevertheless, without density variation in the fluid the flow of aqueous is just the radial flow due to production/drainage of aqueous, whilst with the density variation included the buoyancy driven flows discussed in this article arise, which are 100 times stronger. We anticipate that accounting for variations in viscosity would make a difference in proportion to the variation, that is only around a 6% difference, which is much smaller. We also neglected the haptics, which are fitted with claws at their ends and are used to attach the pIOL to the iris, but as shown by Repetto *et al.* (2015), their inclusion makes little difference to the fluid dynamics.

In the case of the flow generated by aqueous production and drainage the main quantity of interest is the pressure excess generated in the anterior chamber by implantation of the pIOL. Our results show that for this pressure growth to be of clinical significance, the pIOL need to be positioned extremely close to the iris, much closer than it actually is if the device is correctly positioned. We therefore conclude that in

normal circumstances implantation of an iris-fixated pIOL is unlikely to produce a significant pressure increase in the anterior chamber.

Concerning the thermally driven flow, we found, in agreement with previous works (e.g. Canning *et al.*, 2002), that it is much more intense that the one induced by aqueous production/drainage. Although the velocity and pressure distributions change significantly after implantation of the pIOL, they are both the same order of magnitude as before implantation. Unfortunately, typical values of the conductivity of the material of the pIOL are unknown, and our results show that the flow is very sensitive to the value of this conductivity. If it is of the same order of magnitude as that of the aqueous humour, the flow is much smaller than it is with a non-conducting device and the shear stress is reduced by around 30%. Our results are in agreement with previous findings by Niazi *et al.* (2012) and Repetto *et al.* (2015), who used fully numerical approaches, and show, in addition to the findings of these works, that, whatever the value of the thermal conductivity of the pIOL, the wall shear stress on the cornea is smaller than in the absence of the device.

It has been hypothesized that the loss of endothelial cells from the cornea sometimes experienced by patients after pIOL implantation could be due to an increase of the wall shear stress on the cornea. This speculation is not supported by the results of the present study, thus alternative mechanisms should be invoked to explain this clinical finding. If pressure is applied to the cornea, significant corneal indentations can occur, possibly even to the point at which the cornea touches the pIOL. Such contact, if it occurs, is likely to cause significant mechanical friction and, consequently, cell loss. Another possible cause of endothelial cell loss, which was postulated in Repetto *et al.* (2015), could be related to a lack of nutrient delivery to the cornea after pIOL implantation owing to a shielding effect exerted by the device that inhibits normal aqueous flow in the vicinity of the corneal surface. We plan to consider this problem in future work.

Funding

This work was financially supported by Ophtec (BV, Groningen, The Netherlands).

Conflict of interest

P.S. is employed by Ophtec (BV, Groningen, The Netherlands).

References

Abouali, O., Modareszadeh, A., Ghaffarieh, A. & Tu, J. (2012) Investigation of saccadic eye movement effects on the fluid dynamic in the anterior chamber. *ASME J. Biomech. Eng.*, **134**, 021002.

Amini, R. & Barocas, V. H. (2010) Reverse pupillary block slows iris contour recovery from corneoscleral indentation. *ASME J. Biomech. Eng.*, **132**, 071010.

Amini, R., Jouzdani, S. & Barocas, V. H. (2012) Increased iris-lens contact following spontaneous blinking: mathematical modeling. *J. Biomech.*, **45**, 2293–2296.

Batchelor, G. K. (1967) *An Introduction to Fluid Dynamics*. Cambridge: Cambridge University Press.

Beswick, J. A. & McCulloch, C. (1956) Effect of hyaluronidase on the viscosity of the aqueous humour. *Br. J. Ophthamol.*, **40**, 545–548.

Brubaker, R. F. (1989) Measurement of aqueous flow by fluorophotometry. *The Glaucomas* (R. Ritch, MB. Shields & T. Krupin eds). St. Louis: Mosby, 337–344.

Brubaker, R. F. (1991) Flow of aqueous humor in humans (the Friedenwald lecture). *Invest. Ophthalmol. Vis. Sci.*, **32**, 3145–3166.

CANNING, C. R., GREANEY, M. J., DEWYNNE, J. N. & FITT, A. D. (2002) Fluid flow in the anterior chamber of a human eye. *IMA J. Math. Appl. Med.*, **19**, 31–60.

DOORS, M., BERENDSCHOT, T. T. J. M., WEBERS, C. A. B. & NUJITS, R. M. M. A. (2010) Model to predict endothelial cell loss after iris-fixated phasic intraocular lens implantation. *Invest. Ophthalmol. Vis. Sci.*, **51**, 811–815.

EFRON, N., YOUNG, G. & BRENNAN, N. A. (1989) Ocular surface temperature. *Curr. Eye Res.*, **8**, 901–906.

FITT, A. D. & GONZALEZ, G. (2006) Fluid mechanics of the human eye: aqueous humor flow in the anterior chamber. *Bull. Math. Biol.*, **68**, 53–71.

HEYS, J. J. & BAROCAS, V. H. (2002a) A Boussinesq model of natural convection in the human eye and the formation of Krukenberg's spindle. *Ann. Biomed. Eng.*, **30**, 392–401.

HEYS, J. J. & BAROCAS, V. H. (2002b) Computational evaluation of the role of accommodation in pigmentary glaucoma. *Invest. Ophthalmol. Vis. Sci.*, **43**, 700–708.

HEYS, J. J., BAROCAS, V. H. & TARAVELLA, M. J. (2001) Modeling passive mechanical interaction between aqueous humor and iris. *ASME J. Biomech. Eng.*, **123**, 540–547.

HUANG, E. C. & BAROCAS, V. H. (2004) Active iris mechanics and pupillary block: Steady-state analysis and comparison with anatomical risk factors. *Ann. Biomed. Eng.*, **32**, 1276–1285.

HUANG, E. C. & BAROCAS, V. H. (2006) Accommodative microfluctuations and iris contour. *J. Vision*, **6**, 653–660.

JOUZDANI, S., AMINI, R. & BAROCAS, V. H. (2013) Contribution of different anatomical and physiologic factors to iris contour and anterior chamber angle changes during pupil dilation: Theoretical analysis. *Invest. Ophthalmol. Vis. Sci.*, **54**, 2977–2984.

KAWAMORITA, T., UOZATO, H. & SHIMIZU, K. (2012) Fluid dynamics simulation of aqueous humour in a posterior-chamber phakic intraocular lens with a central perforation. *Graefes Arch. Clin. Exp. Ophthalmol.*, **250**, 935–939.

KESTIN, J., SOKOLOV, M. & WAKEHAM, W. A. (1978) Viscosity of liquid water in the range -8°c to 150°c. *J. Phys. Chem. Ref. Data*, **7**, 941–948.

NIAZI, M., ESTEGHAMATIAN, A., ABOUALI, O., GHAFFARIYEH, A. & AHMADI, G. (2012) Numerical study of natural convection in the anterior chamber of human eye with implanted intraocular lens. *Proceedings of the ASME 2012 Summer Heat Transfer Conference HT2012*. New York, USA: American Society of Mechanical Engineers, 1007–1012.

POPPENDIEK, H. F., RANDALL, R., BREEDEN, J. A., CHAMBERS, J. E. & MURPHY, J. R. (1967) Thermal conductivity measurements and predictions for biological fluids and tissues. *Cryobiology*, **3**, 318–327.

PURSLOW, C. & WOLFFSOHN, J. S. (2005) Ocular surface temperature: a review. *Eye Contact Lens*, **31**, 117–123.

RACITI, M. W. & MAJMUDAR, P. A. (2013) Phakic IOLs: Sulcus versus iris–claw versus angle-supported: complications and outcomes. *Curr. Ophthalmol. Rep.*, **1**, 45–49.

REPETTO, R., PRALITS, J. O., SIGGERS, J. H. & SOLERI, P. (2015) Phakic iris-fixated intraocular lens placement in the anterior chamber: effects on aqueous flow. *Invest. Ophthalmol. Vis. Sci.*, **56**, 3061–3068.